

# Quantitative scanning evanescent microwave microscopy and its applications in characterization of functional materials libraries

Chen Gao<sup>1</sup>, Bo Hu<sup>1</sup>, I Takeuchi<sup>2</sup>, Kao-Shuo Chang<sup>2</sup>,  
Xiao-Dong Xiang<sup>3</sup> and Gang Wang<sup>3</sup>

<sup>1</sup> National Synchrotron Radiation Laboratory and Structure Research Laboratory,  
University of Science and Technology of China, Hefei, Anhui 230029,  
People's Republic of China

<sup>2</sup> Small Smart Systems Center, Department of Materials Science and Engineering and Center  
for Superconductivity Research, University of Maryland, College Park, MD 20742, USA

<sup>3</sup> Intematix Corporation, 351 Rheem Blvd, Moraga, CA 94556, USA

E-mail: cgao@ustc.edu.cn

Received 14 April 2004, in final form 22 October 2004

Published 16 December 2004

Online at [stacks.iop.org/MST/16/248](http://stacks.iop.org/MST/16/248)

## Abstract

This paper gives a comprehensive review on the advances in the field of scanning evanescent microwave microscopy, as a high-throughput characterization tool for electrical properties. Theoretical model analyses used for performing quantitative non-destructive characterization of various materials are presented. Examples of applications of the microwave microscopy to the rapid measurements of dielectric/ferroelectric libraries are given.

**Keywords:** combinatorial material science, high-throughput characterization, scanning evanescent microwave microscopy, near-field microscopy, dielectric/ferroelectric materials, dielectric constant, electric impedance

(Some figures in this article are in colour only in the electronic version)

## 1. Introduction

The pioneering work of Xiang and Schultz in 1995 [1] revived the idea of applying the high-throughput strategy to search for novel functional materials, which can be traced back to the works of Kennedy *et al* in 1965 [2] and Hanak [3] in the 1970s. Following their work, this efficient methodology quickly spread to many disciplines of materials science and demonstrated its superiority to the traditional 'one-at-a-time' method in the screening of new superconductors, magnetoresistive materials, luminescent materials, ferroelectrics, dielectric materials, semiconductors, catalysts, polymers, etc [2–20].

There are two major steps in combinatorial materials research: the parallel synthesis and high-throughput characterization. In the first step, samples covering a range

of different compositions are generated on a single substrate using a set of shadow masks or an *in situ* moving mask (for continuous composition spreads) in conjunction with thin film deposition or inkjet delivery techniques. All samples on the substrate are processed simultaneously to form a materials library. The purpose of this step is to create as many compounds as possible in a short period of time under the same synthesis conditions. Following the synthesis, structural and physical properties of the samples in the library are characterized in the second step in order to rapidly extract information about how physical properties vary as a function of composition and/or discover new compounds.

Although a combinatorial materials experiment starts from the parallel synthesis, the availability of appropriate characterization tools limits the applicability of the combinatorial approach. If there are no tools to measure

the physical properties of interest quickly and quantitatively, the high efficiency of synthesis is useless. It is very often the case that the performance of the characterization tools dictates the design of a library and the overall research efficiency.

The basic requirements for a combinatorial characterization technique for a library are: high-throughput, high spatial resolution and high accuracy in quantitative characterization. These requirements are analogous to that of modern microscopy of various physical properties. Generally speaking, existing combinatorial characterization tools can be classified into two categories, the parallel measurement type and the high-speed series type (including raster scanning microscopy).

Through the interaction of electromagnetic waves with materials, a variety of properties of materials can be obtained. For example, luminescence of phosphor can be determined by measuring the visible light spectrum of a material under the illumination of an ultraviolet source. The lattice structure information can be obtained by detecting the diffracted x-ray beam. In most cases, the spatial resolution limited by the diffraction phenomenon (which is determined by the wavelength) meets the requirement of a combinatorial characterization technique because physical separation between different samples in a library is usually larger than the wavelength. These characterization techniques can be implemented in either parallel or scanning modes. One exception to this is the electrical impedance such as dielectric constant at microwave frequencies due to the relatively long wavelength of microwaves. Fortunately, the development of near-field microwave microscopy has provided a means to quantitatively access this key property with very high spatial resolution and throughput.

The near-field microscope can be classified as one type of scanning probe microscopes (SPM). The first scanning probe microscope was probably the evanescent photon microscope envisioned by Syngé in 1928 [21]. In illuminating an object with a point source (referred to as a probe) located a short distance away, he believed that the diffraction limited spatial resolution could be overcome. The fundamental physics of near-field microwaves is as follows: in the microwave frequency region, connecting a microwave (or a RF) source to a metallic surface with a sharp curvature of radius  $R_0 \ll \lambda$  will generate evanescent waves whose wave vectors can go up to  $k_r \sim 1/R_0$  and with spatial resolution power given by  $\sim R_0$ . These evanescent waves only exist near the metal surface, and they decay exponentially away from the surface. Interaction between the metal tip and a sample will change the field configuration near the tip and its equivalent capacitance. All near-field microwave microscopy probes are based on this effect. We, therefore, adopted the name, scanning evanescent wave microscopy, as a more accurate representation of this type of probe.

## 2. Evanescent probe and system design

Fraint and Soohoo independently demonstrated Syngé's idea at microwave frequencies in 1959 and 1962, respectively [22, 23] (although the work by Ash and Nicholls 10 years later [24] is often credited as the first work in the literature). In these works, aperture or tapered waveguide probes were used.

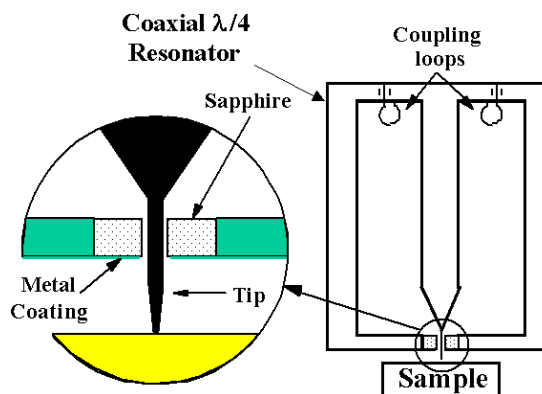


**Figure 1.** Shielded  $\lambda/4$  coaxial resonator probe proposed by Wei and Xiang.

Operating below the cut-off frequency, these probes suffer severely from waveguide decay. Tapered waveguide probes were widely used in NSOM with a typical attenuation of  $10^{-3}$  to  $10^{-6}$ . In these probes, a linear improvement in resolution will cause an exponential reduction in sensitivity as shown by Soohoo [23]. Thus, there is a hard compromise between resolution and sensitivity. Bryant and Gunn were probably the first (1965) to use a tapered coaxial transmission line probe to study the local conductivity of materials (with a spatial resolution of 1 mm) [25]. As there is no cut-off frequency in a transmission line, coaxial transmission line probes have much better performance than aperture or waveguide probes. Fee and Chu, realizing the compromise, suggested using a coaxial transmission line with a small cross section as the non-resonator probe for microwave and infrared regions [26]. Wang *et al* in 1987 and in 1990 demonstrated an evanescent microwave microscope based on a scanning tapered open and closed end of a microstrip resonator, respectively [27]. Microstrip resonators are a type of transmission line, and their open end and close end correspond to an electric dipole and magnetic dipole, respectively. Tabib-Azar *et al* also discussed a similar approach in 1993 [28]. However, as the resolution is mainly determined by the cross section of the transmission line at the open end, shrinking the cross section still causes significant transmission line decay. This is especially true when a long section of a coaxial transmission line is used to form a resonator. If the cross section is wide, the unshielded propagating waves at the open end of the transmission line tend to increase the difficulty of quantitative analysis, since both near-field and far-field interactions have to be considered in this case.

To overcome this problem, the shielded coaxial resonator probe was proposed by Wei and Xiang [29]. As shown in figure 1, a metal tip is mounted on the centre conductor of a high quality factor coaxial resonator. The unique shielding structure is designed to minimize the effect of the propagating waves and maintain the quality factor as high as possible. The shielding structure consists of a sapphire disc with a centre hole of a size comparable to the diameter of the tip wire. The disc is mounted on the end wall of the resonator and a thin silver layer is coated on the outside of the disc. The tip protrudes through the shielding layer to interact with the sample surface. Since most of the transmission line section has a wide cross section, the quality factor of the transmission line resonator is



Figure 2. A photo of an EMP 2003 system.

very high, thereby providing an increased detection sensitivity. At the same time, because the propagating waves are shielded within the resonator, only evanescent waves interact with a sample at the tip. The interaction between the tip and a sample, reflecting the sample complex electrical impedance, is measured as changes in the resonant frequency  $f_r$  and quality factor  $Q$  of the resonator. A commercial system has been developed based on this probe design (EMP-2003, Intematix Corporation, 351 Rheem Blvd, Moraga, CA 94556, USA). Shown in figure 2 is a photo of the commercial system and figure 3 illustrates the details of the microscope.

In order to perform quantitative microscopy of various materials properties while preventing damage to the sharpened tip and the sample surface, the tip-sample distance needs to be controlled during the raster scan. This is because the microscopy signal is a convolution of topography and physical properties. Separating the two signals requires measuring at least two independent signals simultaneously. In the system shown in figure 4, an atomic force microscope (AFM) is integrated to regulate the tip-sample distance. Using this, the tip position can be controlled at a distance from the sample surface at angstrom level, and the topography of the sample can be obtained simultaneously with electric impedance.

To map the sample impedance, topography or other information, this system provides five imaging modes and one metrology mode with many sub-mode settings.

- (1) *Constant resonant frequency ( $f_r$ ) mode*: This mode is the most useful for characterization of conducting materials. Using the change in resonant frequency as a feedback control signal for the  $z$ -axis maintains the tip-sample distance while the  $x$ - $y$  stage or a piezoelectric scanner rasters the tip over the sample surface. The system obtains the quality factor image to obtain conductivity

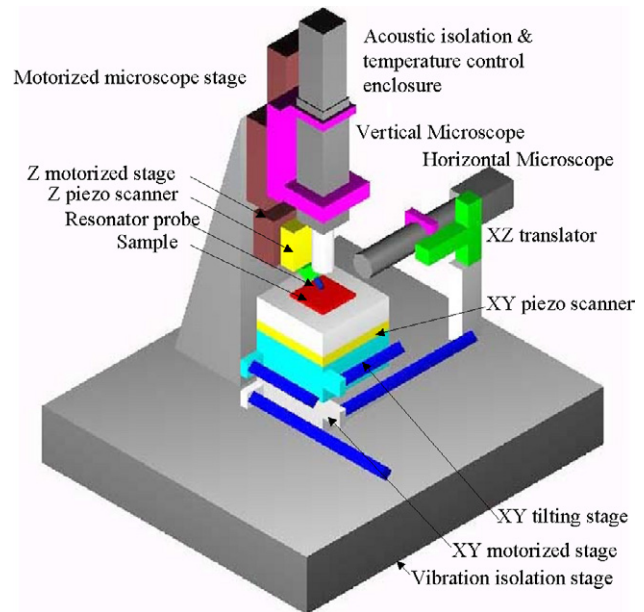


Figure 3. Function blocks of an EMP 2003 probe and stage system.

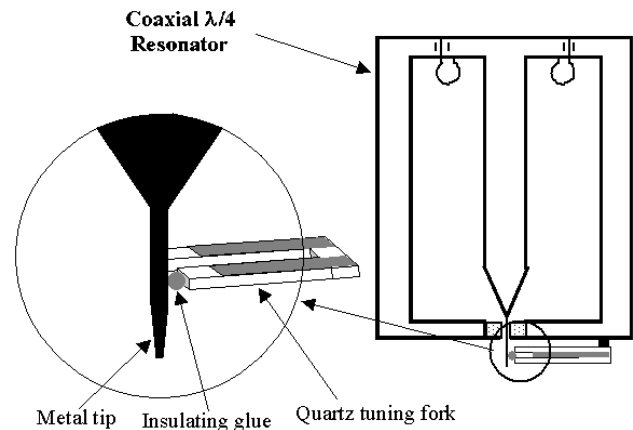
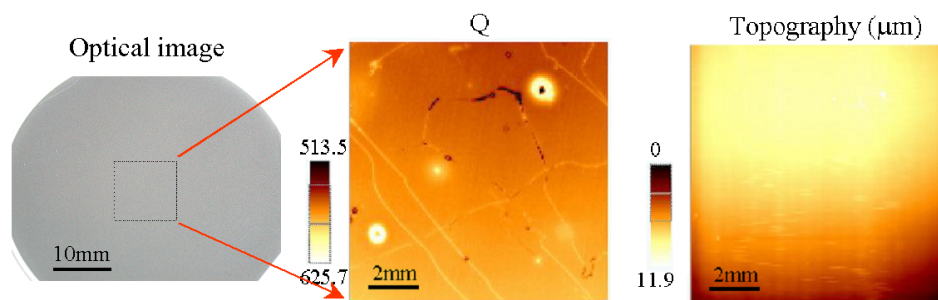


Figure 4. AFM incorporated in SEMM.

or sheet resistance information. 'Topography image' can be obtained by recording the feedback control voltage of the  $z$ -axis nano-positioning device. Figure 5 demonstrates a typical scan image obtained using this mode.

- (2) *Constant force imaging mode*: Using the detected force from an integrated force sensor as the feedback signal for the  $z$ -axis while the tip scans over the sample surface, resonant frequency and quality factor images are recorded to obtain information on the dielectric constant and the loss tangent of dielectric materials. The feedback controlled  $z$ -axis position can be plotted as topography images. Figure 6 displays a typical scan image obtained using this mode.
- (3) *Contact mode*: The tip is in soft contact with the sample surface during the data acquisition. The soft contact could be realized by mounting the sample on the soft contact stage. 'Resonant frequency and quality factor images' are recorded to obtain information on the dielectric constant and the loss tangent of dielectrics.
- (4) *Constant height mode*: This is similar to AFM operation. The tip scans over the sample surface with an open loop



**Figure 5.** Defect inspection of a GaN wafer under the constant frequency mode. The defect is clearly shown in the  $Q$  image but cannot be seen in a simultaneously obtained topography image and an independently obtained optical image.

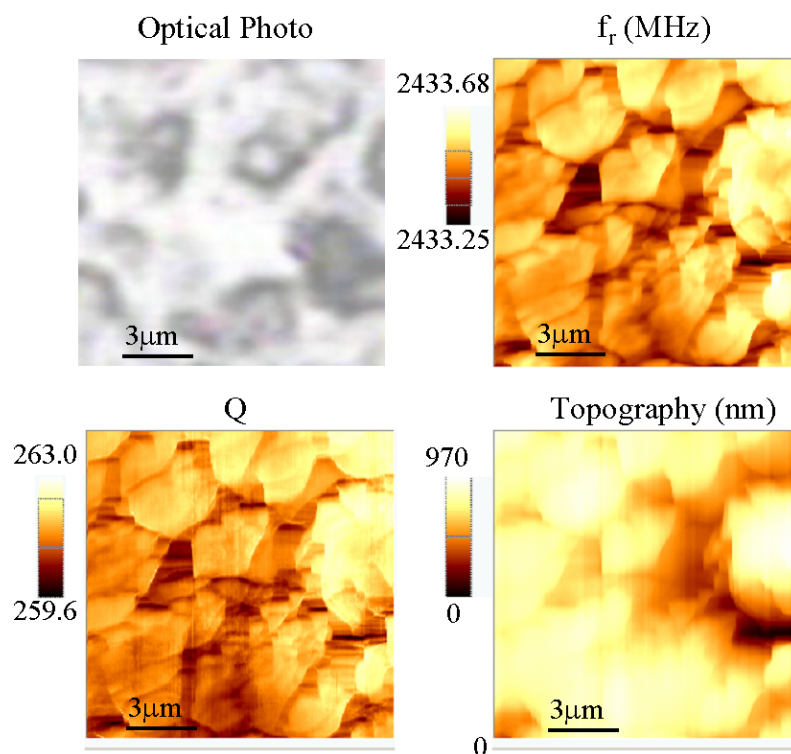


**Figure 6.** Simultaneously obtained impedance and topography images of a fine polished ceramic surface. The optical photograph is taken separately for comparison.

$z$ -axis control. Data acquisition rate can be as fast as 100 kHz with this mode.

- (5) *Bias mode*: A bias voltage for modulating the resonant frequency is applied between the tip and a bottom electrode in the sample. Modulating signals in  $f_r$  or  $Q$  can be recorded to obtain nonlinear dielectric constant information. Figure 7 shows a typical scan image obtained using this mode.
- (6) *Metrology mode*: Using the  $z$ -axis nano-positioning device, the system can perform automated tip-sample approaching curve measurements where various parameters are recorded as the tip-sample distance is decreased. Fitting the approach curve can provide measurements at selected locations without contacting the sample surface. The locations can be a single point, multiple points, a 1D array or a 2D matrix of points. A reference value of  $f_r$  or force can be used effectively as the targets corresponding to a fixed tip-sample distance. Figure 8 shows examples of tip-sample approaching curves fitted to the theory.

Very recently, Aga and his colleagues [30] have constructed a dual channel microscope, as shown in figure 9. They have replaced the metal tip of a coaxial cable SEMM with a metallized tapered optic fibre tip (SNOM tip), so that the optical and dielectric properties can be accessed simultaneously. We believe that this new design can be adapted to other type of SEMMs and should find applications in the high-throughput characterization of materials libraries, especially in the search for novel opto-electronic and electro-optical materials with the combinatorial approach.

### 3. Quantitative microscopic theory and comparison to experimental data

The main difficulty of near-field microscopy lies in the quantitative capability. A sound quantitative near-field microscopy theory must consider the probe and sample as a whole system, and solve the wave equations under real boundary conditions to obtain the field distribution. Numerical

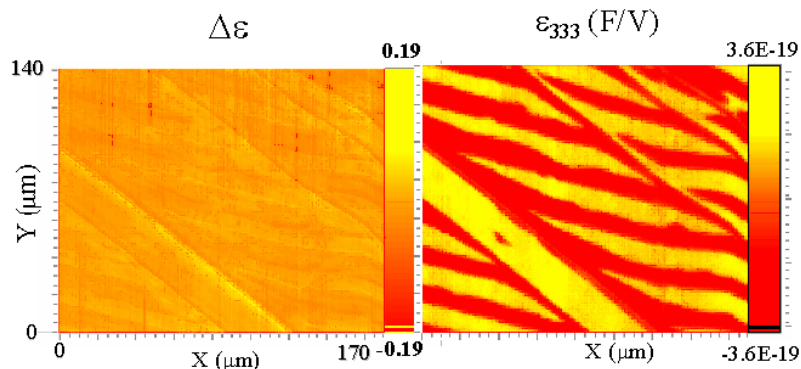


Figure 7. Simultaneous imaging of linear (relative) and nonlinear dielectric constants of LiNbO<sub>3</sub>.

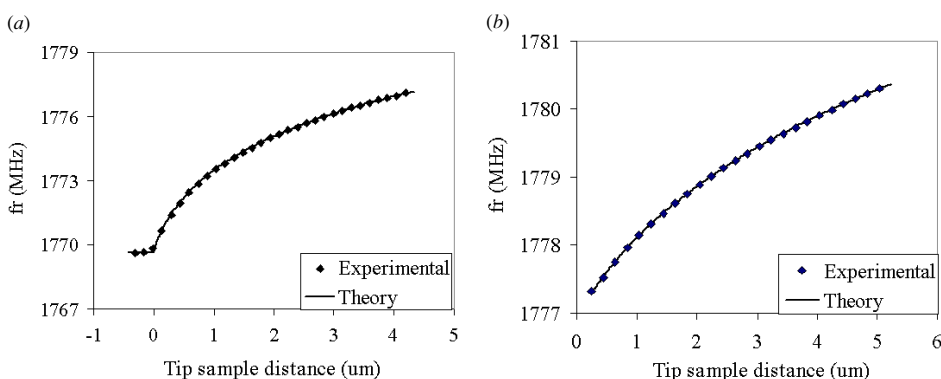


Figure 8. Approach curve fitting of (a) LaAlO<sub>3</sub> and (b) MgO single crystals.

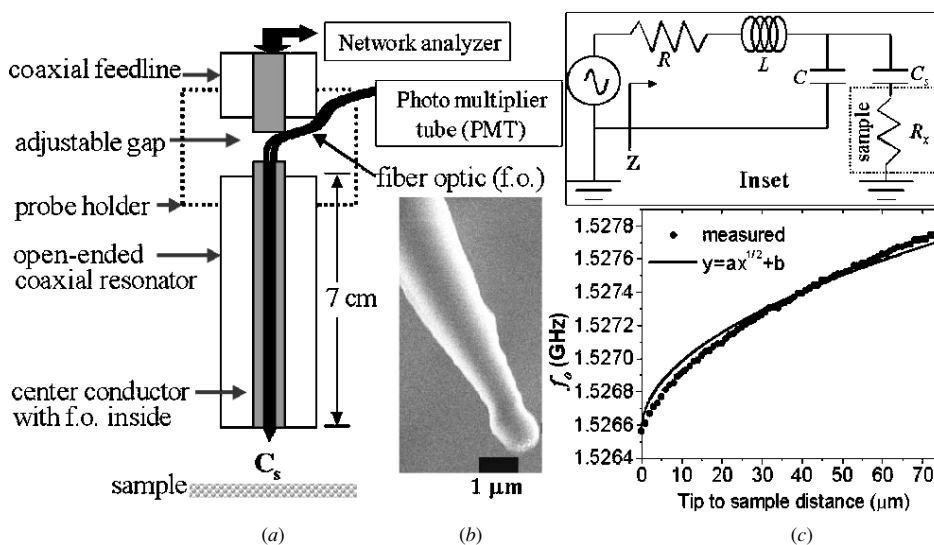


Figure 9. SEMM and SNOM dual channel microscope designed by Aga (reprinted from [30]).

methods are often involved [31]. Although a number of numerical simulation softwares are available commercially and have been applied to many applications, it is hard for them to simulate the field in the near-field microscope accurately [32]. Since the tip is sharply curved, a rapidly varying mesh size has to be implemented. Even when a variable mesh technique is used, the number of nodes required for an accurate simulation of such a fast amplitude-varying field is still too large, and not practical in routine applications.

By assuming the quasi-static approximation and modelling the tip-sample interaction properly using the image-charge method, Gao and Xiang obtained analytic solutions of the electric field near the tip for bulk materials in 1997 [33–35]. Based on the field distribution, they calculated the shifts of the resonant frequency and the quality factor of the resonator probe due to the tip-sample interaction and derived the dielectric constant and the loss tangent of samples quantitatively with simple boundary conditions.

These theoretical results were soon confirmed by a few groups independently with experiments and numerical simulations [36–38]. They have been successfully used in the high-throughput characterization of dielectric materials libraries [13, 15, 20, 39–44]. Most recently, Gao *et al* proposed self-similar tree-like image charges to address the thin film sample case more accurately. A recursive algorithm has been developed to calculate the total charges on the tip–film–substrate system and used to derive the dielectric constant and the thickness of the film [32]. We believe this progress will have a significant impact on the combinatorial studies of electronic materials because the natural form of electronic materials is a thin film.

Two critical approximations were made in obtaining these analytical solutions [33, 34]: (1) spherical tip: because the main part of the probe interacting with the sample is the tip cap; this is a good approximation, especially when the probe is held at a distance from the sample shorter than the probe radius; (2) quasi-electrostatic: because the effective region with significant non-zero field distribution is several orders smaller than the relative long wavelength of the microwave, the phase effect can be neglected.

Under the above approximations, the problem is simplified to solving the static electric field distribution in the sample under two boundary conditions: equipotential surface of the sphere and continuity at the sample surface. The field can be solved in many manners. A straightforward way is the charge image method. The quantitative relations relate the tip radius ( $R_0$ ), tip–sample distance ( $g$ ) and real and imaginary dielectric constant. Geometrical constants can be determined by proper calibration. We will discuss some specific examples and compare the theoretical results with experimental data in the following sections.

### 3.1. Modelling of the probe response for bulk dielectric materials

The complex dielectric constant of a thick sample can be determined by an image charge approach (assuming its thickness is infinite). For dielectric samples, the dielectric constant is largely real, or the loss tangent ( $\tan \delta$ ) is small:

$$\varepsilon = \varepsilon_r + i\varepsilon_i \approx \varepsilon_r \quad \tan \delta = \frac{\varepsilon_i}{\varepsilon_r} < 0.1 \quad (1)$$

where  $\varepsilon_r$  and  $\varepsilon_i$  are the real and imaginary parts of the dielectric constant ( $\varepsilon$ ) of the sample, respectively. The charge redistribution on the tip caused by the probe–sample interaction can be represented by a series of iterative image charges as shown in figure 10 [33, 34]:

$$a_n = \begin{cases} 1 + a - \frac{1}{1 + a + a_{n-1}} & g > 0 \\ \frac{1}{n} & g = 0 \end{cases} \quad (n \geq 2), \quad (2)$$

$$t_n = \begin{cases} \frac{b}{1 + a + a_{n-1}} t_{n-1} & g > 0 \\ \frac{b^{n-1}}{n} & g = 0 \end{cases}$$

where  $t_n$  and  $a_n$  are the magnitude of the  $n$ th image charge and its distance from the sample surface in units  $q_1$  ( $q_1 = 4\pi\varepsilon_0 R_0 V_0$ , where  $V_0$  is the open end voltage of the resonator)

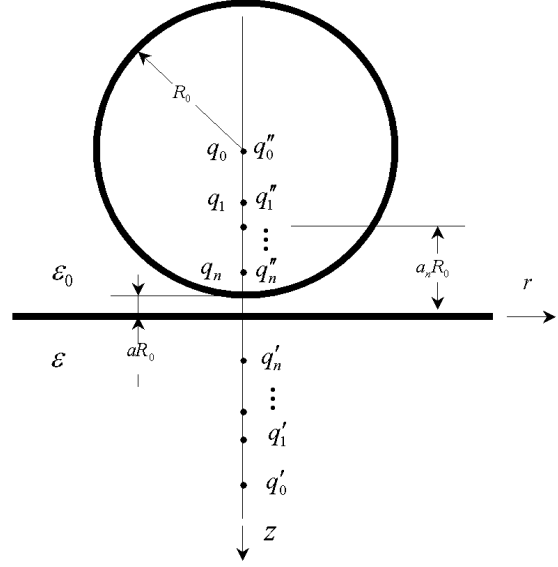


Figure 10. The iterative image charges in tip–bulk sample system.

and  $R_0$  (the tip radius), respectively.  $b = \frac{\varepsilon - \varepsilon_0}{\varepsilon + \varepsilon_0}$  ( $\varepsilon$  and  $\varepsilon_0$  are the permittivities of the sample and the free space, respectively) and  $g = aR_0$  is the probe–sample distance as also shown in figure 10. The initial conditions for the iterations are:  $a_1 = 1 + a$ ,  $t_1 = 1$ .

Since the majority of the microwave energy is shielded inside the resonator and the probe–sample interaction almost does not change the field distribution in the cavity, the frequency and quality factor shifts of the resonator can be calculated with perturbation theory [45] by considering the appearance of the sample as a small perturbation to the resonant system [34]:

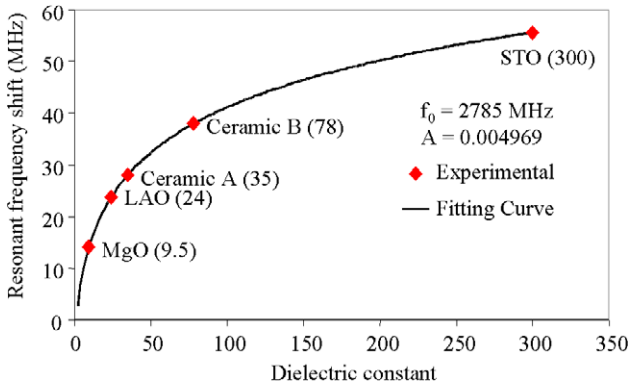
$$\frac{\Delta f_r}{f_r} = \frac{f_r - f_0}{f_r} = \begin{cases} -A \sum_{n=1}^{\infty} \frac{bt_n}{a_1 + a_n} & g > 0 \\ A \left[ \frac{\ln(1-b)}{b} + 1 \right] & g = 0 \end{cases} \quad (3)$$

$$\Delta \left( \frac{1}{Q} \right) = \frac{1}{Q} - \frac{1}{Q_0} = -(B_Q + B'_Q \tan \delta) \frac{\Delta f_r}{f_r}$$

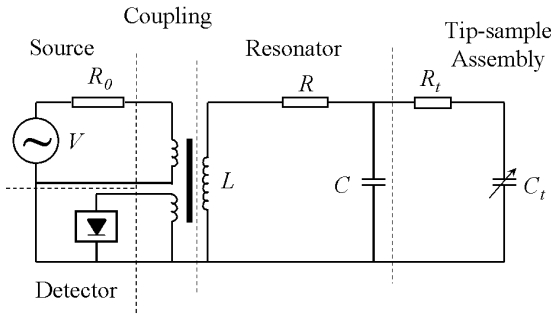
where  $A$ ,  $B_Q$  and  $B'_Q$  are constants determined by the geometry of the tip–resonator geometry, and  $f_0$  and  $Q_0$  are the resonant frequency and quality factor of the resonator without a sample present near the tip, respectively.

Figure 8 in the previous section shows measured approaching curves on single crystals of  $\text{LaAlO}_3$  (LAO) and  $\text{MgO}$  fitted to theoretical results. The agreement between theory and experimental data is excellent (with a fitting error  $< 10^{-6}$ ). Using this method, we can routinely obtain a precise value of  $\varepsilon$ . Figure 11 shows a comparison between the experimentally determined dielectric constant of various samples (measured independently by a conventional dielectric resonator method [46]) and theoretical results (solid line) plotted as the change in resonant frequency versus dielectric constant.

$B_Q$  and  $B'_Q$  terms in equation (3) represent the dielectric loss of samples and the loss from the extra current required to support the charge redistribution on the tip. Experimentally, constants  $B_Q$  and  $B'_Q$  are a good approximation for sharp tip and low loss dielectric materials, however, in reality  $B_Q$



**Figure 11.** Experimental data and theoretical fitting for the change in resonant frequency as a function of relative dielectric constant.



**Figure 12.** The equivalent lumped resonant circuit for SEMM.

and  $B'_Q$  show considerable frequency and dielectric constant dependence. For this reason, careful calibration of the system is a major problem in the experimental determination of the loss tangent to the level below  $10^{-2}$ .

### 3.2. Equivalent circuit analysis

The resonator (here, specifically for an ideal quarter-wave resonator with lossless cavity material) can be analysed using an equivalent lumped series resonant circuit as shown in figure 12 with effective capacitance  $C$ , inductance  $L$  and resistance  $R$ :

$$\begin{cases} C = \frac{2\pi\epsilon_r}{\ln(R_2/R_1)}l \\ L = \frac{\mu_r}{2\pi}l \ln(R_2/R_1) \\ R = \frac{R_s}{2\pi} \left[ \left( \frac{1}{R_2} + \frac{1}{R_1} \right)l + \ln \left( \frac{R_2}{R_1} \right) \right], \end{cases} \quad (4)$$

where  $l \approx \lambda/4$  is the effective cavity length,  $R_s$  is the surface resistance of the wall metal of the cavity,  $R_2$  and  $R_1$  are the radii of the outer and centre conductors, respectively;  $\epsilon_r$  and  $\mu_r$  are the permittivity and permeability of the cavity material, respectively.

In this model, the tip sphere can be considered as a small stand-alone capacitor  $C_t$  in parallel with  $C$  through the series resistor  $R_t$  of the tip wire. The probe-sample interaction increases the tip sphere capacitance by increasing the charges on the sphere while its voltage is kept constant, and the resonant frequency shift of the system should be proportional to the summation of the image charges caused by the probe-sample interaction:

$$\frac{\Delta f_r}{f_r} = \frac{\Delta C_t}{2C} = -A \sum_{n=2}^{\infty} q_n. \quad (5)$$

### 3.3. Modelling of the probe response for thin dielectric films on dielectric substrate

As most dielectric/ferroelectric materials libraries are fabricated in thin film formats, a quantitative theory for the thin film dielectric constant is extremely desirable. However, the boundary condition for the image charge method becomes more complex due to the divergence of the image charges. Under conditions that the film dielectric constant is high relative to the substrate, the contribution from the substrate will decrease fast and the following approximation can be used to replace the effect of the reaction from the complicated image charges with an effective charge [34]:

$$b_{\text{eff}} = b_{20} + (b_{10} - b_{20}) \exp \left( -D \frac{a}{1 - b_{20}} \right) \quad (6)$$

where  $b_{20} = \frac{\epsilon_2 - \epsilon_1}{\epsilon_2 + \epsilon_1}$  and  $b_{10} = \frac{\epsilon_1 - \epsilon_0}{\epsilon_1 + \epsilon_0}$ ,  $\epsilon_2$  and  $\epsilon_1$  are the dielectric constants of the film and the substrate, respectively,  $a = \frac{t}{R_0}$ , and  $t$  is the thickness of the film. The coefficient  $D$  can be calibrated from a standard sample. Gao and Xiang [34] had obtained  $D = 0.18$  by calibrating against interdigitated electrode measurements at the same frequency on a SrTiO<sub>3</sub> thin film. It is conceivable that  $D$  takes different values in different ranges of dielectric constant.

By using the approximation in equation (6), the following relation can be derived:

$$\begin{aligned} \frac{\Delta f_r}{f_r} &= -A \sum_{n=1}^{\infty} \sum_{m=0}^{\infty} b_{\text{eff}}^{n-1} b_{21}^m b_{10}^m \\ &\times \left( \frac{b_{20}}{n+1+2mna} - \frac{b_{21}}{n+1+2(m+1)na} \right) \\ \Delta \left( \frac{1}{Q} \right) &= A \sum_{n=1}^{\infty} \sum_{m=0}^{\infty} b_{\text{eff}}^{n-1} b_{21}^m b_{10}^m \\ &\times \left( \tan \delta_2 \left( \frac{1}{n+1+2mna} - \frac{1}{n+1+2(m+1)na} \right) \right. \\ &\quad \left. + \frac{2\epsilon_1\epsilon_2 \tan \delta_1}{(\epsilon_2 + \epsilon_1)(\epsilon_2 + \epsilon_0)} \frac{1}{(n+1+2(m+1)na)} \right) - B \left( \frac{\Delta f}{f_0} \right), \end{aligned} \quad (7)$$

where  $b_{21} = \frac{\epsilon_2 - \epsilon_1}{\epsilon_2 + \epsilon_1}$ ,  $\tan \delta_2$  and  $\tan \delta_1$  are the loss tangents of the film and the substrate [34].

Though some results have been obtained using equation (7), there are also several problems with this method. First, the calculation is complicated. It involves 2D iterations even though an approximation has been used. Second, the approximation is not good enough to reflect the charge redistribution in the tip and the sample accurately. Even with the use of  $D$  to accommodate different film-substrate combinations, the experimental result still shows a relatively large systematic error.

Because the FEA method has the potential to simulate the field distribution where the dielectric constant is a function of position, in principle there are no obstacles in extending the application of FEA to the thin film case. Steinhauer *et al* [36] and Lee *et al* [37] have used this method. In particular, Lee *et al* fitted the frequency shift calculated from the field distribution with an empirical formula:

$$-\frac{\Delta f_r}{f_0} = A \left( \frac{p_1}{p_2(g/R_0)^{p_3} + p_4(g/R_0) + 1} \right) + F, \quad (8)$$

where  $p_1$ ,  $p_2$ ,  $p_3$ ,  $p_4$  are fitting parameters, whose descriptions can be found in their paper.

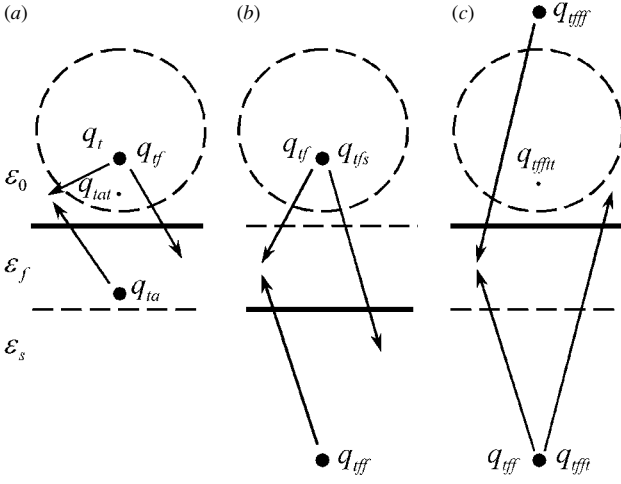


**Figure 13.** Schematic for the recursive image charge process for a thin film sample.  $\varepsilon_f$  and  $\varepsilon_s$  are the dielectric constants of the thin film and the substrate, respectively.

Very recently, Gao and his co-worker successfully extended the charge image method to the thin dielectric film case and introduced an algorithm to calculate the image charges on the tip [32].

A significant difference between thin film and bulk materials is the appearance of the third boundary—the film/substrate interface. It is this interface that changes the image charge process from iterative into recursive as shown in figure 13. The iterative relations are:

$$\begin{cases} q_{\text{tat}} = \frac{R_0}{g+R_0+d_t} b_{f0} q_t \\ d_{\text{tat}} = g + R_0 - \frac{R_0^2}{g+R_0+d_t}, \end{cases} \quad (9)$$

$$\begin{cases} q_{\text{tf}} = (b_{f0} + 1) q_t \\ d_{\text{tf}} = d_t, \end{cases} \quad (10)$$

$$\begin{cases} q_{\text{tffit}} = \frac{R_0}{g+R_0+d_{\text{tf}}+2t} (b_{f0} - 1) b_{fs} q_{\text{tf}} \\ d_{\text{tffit}} = g + R_0 - \frac{R_0^2}{g+R_0+d_{\text{tf}}+2t}, \end{cases} \quad (11)$$

and

$$\begin{cases} q_{\text{tfff}} = b_{fs} b_{f0} q_{\text{tf}} \\ d_{\text{tfff}} = d_{\text{tf}} + 2t \end{cases} \quad (12)$$

with initial conditions:

$$\begin{cases} q_t^{\text{root}} = q_1 \\ d_t^{\text{root}} = g + R_0 \end{cases} \quad (13)$$

where  $b_{fs} = \frac{\varepsilon_f - \varepsilon_s}{\varepsilon_f + \varepsilon_s}$ ,  $b_{f0} = \frac{\varepsilon_f - \varepsilon_0}{\varepsilon_f + \varepsilon_0}$ ,  $\varepsilon_f$  and  $\varepsilon_s$  are the dielectric constants of the film and that of the substrate, respectively.

The frequency shift of the resonator can be calculated by summing up the image charges on the tip sphere until the magnitude of the image charge is infinitely small. However, as the efficiency of the standard recursive algorithm is low, they implemented a recursive to circulation conversion. This new algorithm improves the computation efficiency by a factor of 10, and extends the computable range to about 0.001 of the  $t/R_0$  ratio.

Figure 14 is the calculated charge increment caused by the tip–film/substrate interaction as functions of the film

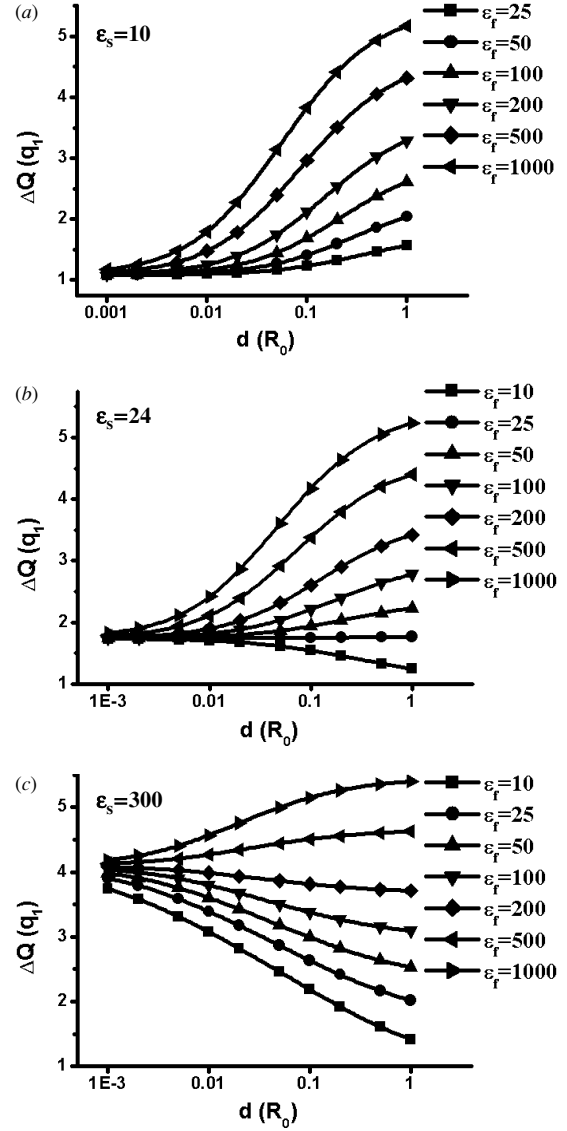


**Figure 14.** The charge increment on the tip  $\Delta Q$  as a function of film thickness  $d$ , different relative dielectric constant of the film ( $\varepsilon_f$ ) and substrate ( $\varepsilon_s$ ). The units of  $\Delta Q$  and  $d$  are the root charge  $q_1$  and tip radius  $R_0$ , respectively.

thickness, dielectric constants of the film and the substrate. The overall trends of the results are fairly consistent with that obtained from FEA.

#### 4. Applications of scanning evanescent microwave microscopy in combinatorial materials research

An important property of dielectric materials is the complex dielectric constant. For example, high dielectric constant and low loss materials are highly desirable for applications in DRAM, FRAM and wireless communication devices. Researchers have spent much effort in identifying such materials.  $(\text{Ba}_x\text{Sr}_{1-x})\text{TiO}_3$  (BST) has been considered to be a good candidate material. Although various compositions of BST had been studied by many groups [48–51], systematic and comprehensive studies of the dopants' effects on the properties of BST were lacking. To this end, Xiang and

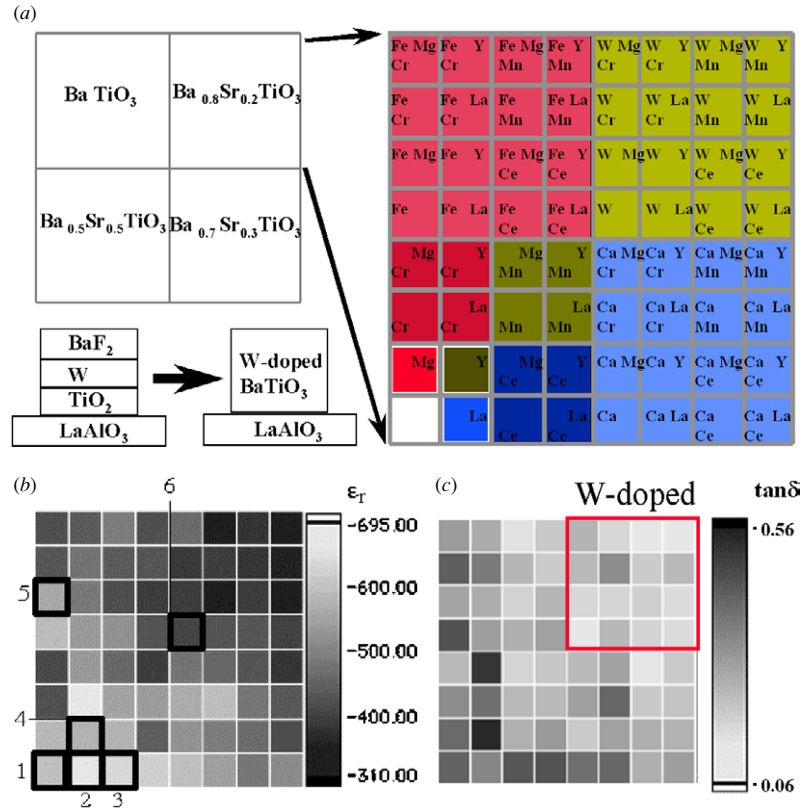


**Figure 15.** (a) Dopant map and synthesis schematic of the doped  $\text{Ba}_x\text{Sr}_{1-x}\text{TiO}_3$  library, (b) relative dielectric constant and (c) loss tangent images of the library.

co-workers fabricated a doped  $\text{Ba}_x\text{Sr}_{1-x}\text{TiO}_3$  ( $x = 1.0, 0.8, 0.7,$  and  $0.5$ ) thin film materials library [14]. By combining RF sputtering and quaternary mask techniques, a library consisting of four hosts with different combinations of dopants (up to three out of nine metallic elements of Fe, Mg, Cr, Mn, W, Ca, Y, La and Ce where each dopant is added in excess of 1 mol% with respect to the BST host) was deposited on a 1 inch  $\times$  1 inch (100)  $\text{LaAlO}_3$  single crystal substrate. Its composition map is shown in figure 15(a). BST was synthesized from  $\text{TiO}_2$ ,  $\text{BaF}_2$  and  $\text{SrF}_2$ . The deposition steps were as follows. First, a layer of  $\text{TiO}_2$  (870 Å) was deposited on all sample sites of the library. Layers of  $\text{BaF}_2$ ,  $\text{SrF}_2$  and dopants were then deposited in the sequence of:  $\text{Fe}_2\text{O}_3$  (7 Å), W (5 Å),  $\text{CaF}_2$  (12 Å), Cr (4 Å),  $\text{Mn}_3\text{O}_4$  (7 Å),  $\text{CeO}_2$  (12 Å),  $\text{MgO}$  (7 Å),  $\text{Y}_2\text{O}_3$  (10 Å),  $\text{La}_2\text{O}_3$  (12 Å),  $\text{BaF}_2$  (1640 Å),  $\text{SrF}_2$  (270 Å) +  $\text{BaF}_2$  (1320 Å),  $\text{SrF}_2$  (410 Å) +  $\text{BaF}_2$  (940 Å),  $\text{SrF}_2$  (680 Å) +  $\text{BaF}_2$  (830 Å), so that the dopant layers were sandwiched in between the bottom  $\text{TiO}_2$  and the fluorides to avoid their possible evaporation during the post annealing. Before the final sintering in oxygen at 900 °C, the library was pre-heated to 400 °C for 24 h in a flowing oxygen atmosphere to facilitate mixing of the precursors. Careful post annealing (controlled solid state reaction) produced high quality epitaxial thin film samples in the library, which were confirmed by x-ray diffraction ( $\phi$  scan) and Rutherford back scattering (RBS).

Shown in figures 15(b) and (c) are the dielectric constant and the loss tangent mapping of the samples on the library measured using SEMM at 1 GHz. Here the dielectric constant and loss tangent are averaged within each sample. From the

images, a low loss region with a reasonable large dielectric constant was identified as samples doped with W (upper right hand quadrant). Other findings from the library include the fact that most dopants decrease the dielectric constant except La and Ce. Relatively larger ion dopants such as La tend to result in higher dielectric constant, but this effect is less pronounced if the host contains Sr.

To confirm these results, individual film samples were fabricated for selected compositions identical to those sites in the library, and their dielectric properties were measured using the interdigital contact electrode method at 1 MHz. Similar trends to the findings in the library were observed in these samples.

Speculating that the additional  $\text{CaTiO}_3$  may further reduce the loss of BST, Xiang and co-workers deposited a  $(\text{Ba}_{1-x-y}\text{Sr}_x\text{Ca}_y)\text{TiO}_3$  thin film ternary composition spread on an equilateral triangle shaped (100)  $\text{LaAlO}_3$  substrate (1 inch in height) [16]. The deposition was performed using a pulsed laser ablation (PLD) system in conjunction with a high-precision *in situ* linear shutter. A linear film thickness gradient on the substrate can be formed by ablating the precursor target uniformly while moving the shutter across the substrate with a constant speed. The deposition steps were as follows: first, 750 Å  $\text{TiO}_2$  was deposited on the entire substrate, then 0–1255 Å  $\text{CaCO}_3$  layer, 0–1475 Å  $\text{SrCO}_3$  layer and 0–1647 Å  $\text{BaCO}_3$  layer were deposited along three altitudes of the equilateral triangle, as shown in figure 16(a). Process conditions and characterization similar to those used for the dopant library were used to process the composition spread.

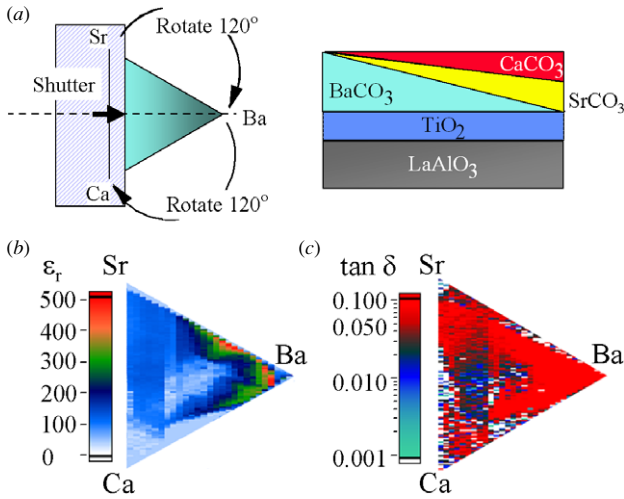


**Figure 16.** (a) Schematic of the deposition scheme of the  $(\text{Ba}_{1-x-y}\text{Sr}_x\text{Ca}_y)\text{TiO}_3$  ternary library, (b) relative dielectric constant and (c) loss tangent images of the library.

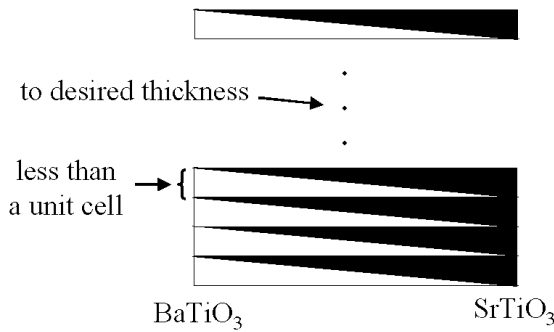


**Figure 17.** Schematic of the deposition of a multilayer composition spread.

The result of the dielectric property mapping is shown in figures 16(b) and (c).

From the mapping, the following findings were obtained:

- $(\text{Ba}_{0.12-0.25}\text{Sr}_{0.35-0.47}\text{Ca}_{0.32-0.53})\text{TiO}_3$  was identified as the region with low loss (loss tangent  $< 0.02$ ) and relatively high dielectric constant (130–160);
- Dielectric constant in  $(\text{Sr}_{1-x}\text{Ca}_x)\text{TiO}_3$  and  $(\text{Ba}_{1-x}\text{Ca}_x)\text{TiO}_3$  systems decreases with increasing amount of Ca;
- $(\text{Ba}_{0.5-0.7}\text{Sr}_{0.3-0.5})\text{TiO}_3$  has the highest dielectric constant (500), and  $\text{SrTiO}_3$  has the lowest dielectric constant (150) in the  $(\text{Ba}_{1-x}\text{Sr}_x)\text{TiO}_3$  system.

Takeuchi and co-workers have used the multilayer composition spread approach to fabricate high quality epitaxial composition spreads of BST [39] (figure 17). In this deposition scheme, alternating thickness gradient wedges of BTO and STO were deposited on the (100)  $\text{LaAlO}_3$  substrate held at  $800^\circ\text{C}$ . Keeping the thickness of each layer less than a unit cell everywhere, the intermixing of BTO and STO was significantly enhanced, and *in situ* epitaxial growth of  $\text{Ba}_{1-x}\text{Sr}_x\text{TiO}_3$  thin film composition spread on (100)  $\text{LaAlO}_3$  was confirmed by x-ray diffraction, RBS and high-resolution cross-sectional transmission electron microscopy.

The dielectric properties of the spread were characterized using a SEMM, and the results agree with the known bulk dielectric properties of BST: the dielectric constant peak

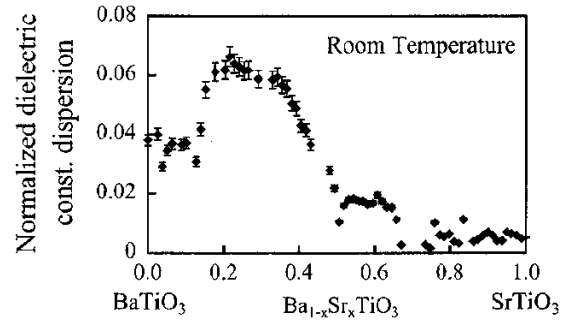


**Figure 18.** Dielectric dispersion measured in the  $\text{Ba}_x\text{Sr}_{1-x}\text{TiO}_3$  system.

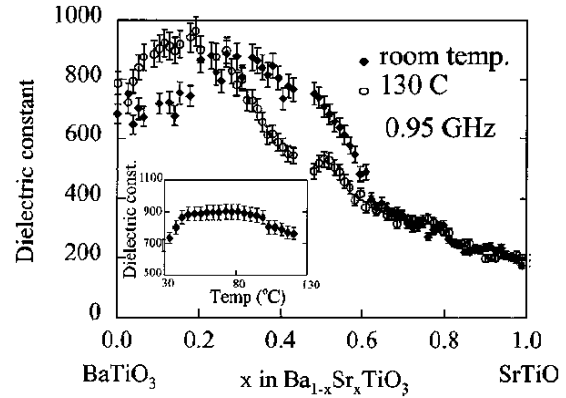


**Figure 19.** Relative dielectric constant of a  $\text{Ba}_x\text{Sr}_{1-x}\text{TiO}_3$  library at room temperature and  $130^\circ\text{C}$ .

appears near  $\text{Ba}_{0.65}\text{Sr}_{0.35}\text{TiO}_3$ , which has its Curie point near room temperature, and the loss increases with the decreasing amount of Sr. As shown in figure 18, they also studied the frequency dispersion of the BST system using the harmonics of the SEMM resonator. They found that the dispersion is close to zero near the STO end, and increases with increasing Ba content and decreases again as  $x$  approaches zero. The maximum dielectric dispersion is around  $x = 0.2-0.4$ . This is consistent with the soft mode behaviour of a paraelectric–ferroelectric transition.

Moreover, they also measured the temperature dependences of the dielectric properties (as shown in figure 19) by adapting a simple coil heater into the sample holder of the SEMM. It reveals that the highest dielectric constant composition shifts to lower Sr composition at increased temperature (from  $\text{Ba}_{0.65}\text{Sr}_{0.35}\text{TiO}_3$  at room temperature to  $\text{Ba}_{0.8}\text{Sr}_{0.2}\text{TiO}_3$  at  $130^\circ\text{C}$ ).

Since most electronic devices are fabricated on Si, Minami and his colleagues further studied the dielectric properties of BST grown on a (100) Si substrate as a function of the growth temperature using the layer by layer combinatorial PLD [41]. They focused a Nd:YAG laser beam on one edge of the substrate holder, so that a linear temperature gradient from  $585^\circ\text{C}$  to  $765^\circ\text{C}$  along the longitudinal direction of the substrate was obtained on the specially designed sample holder during the PLD deposition. Dielectric properties mapped using SEMM are shown in figure 20, and a region with high dielectric constant and low loss ( $0.4 < x < 0.7$  and  $710^\circ\text{C} < T_{\text{gr}} < 750^\circ\text{C}$ ) was identified.

A similar approach has been used to optimize the composition and the growth temperature of  $\text{LiNb}_{1-x}\text{Ta}_x\text{O}_3$  thin

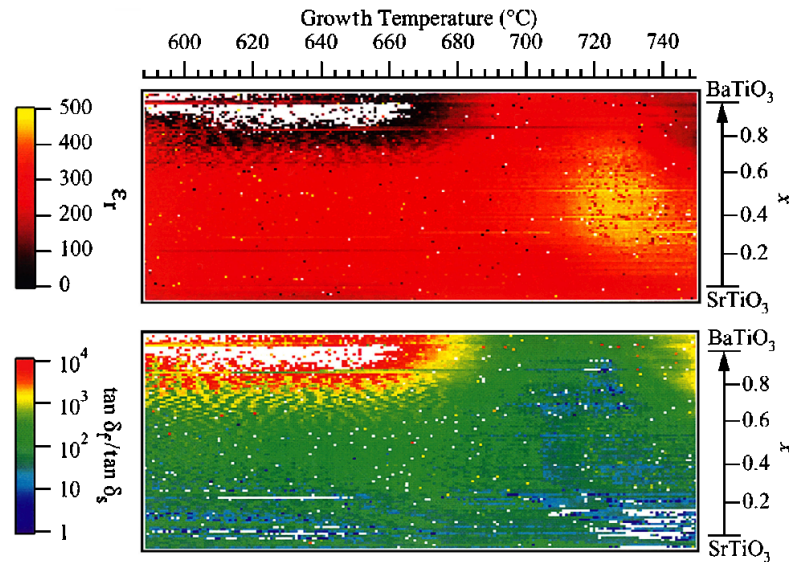


**Figure 20.** (a) Relative dielectric constant and (b) relative tangent loss images of a BST binary library grown at different temperatures (reprinted from [41]).

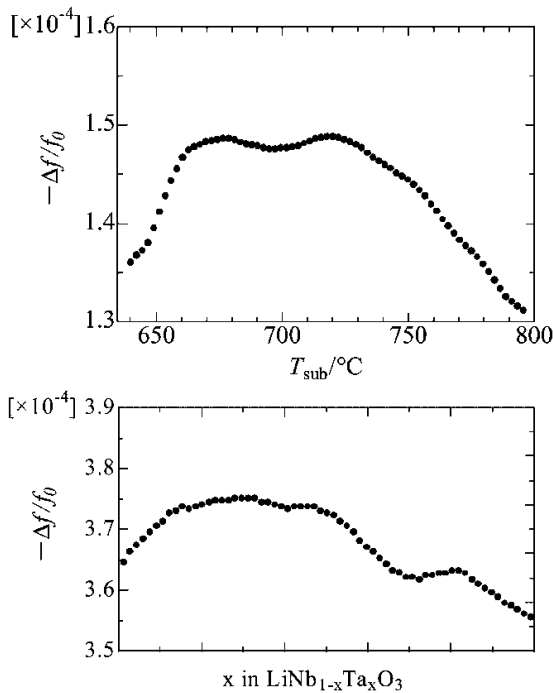


**Figure 21.** SEMM signal as a function of (a) the growth temperature of  $\text{LiNbO}_3$  on the sapphire substrate, and (b) composition in  $\text{LiNb}_{1-x}\text{Ta}_x\text{O}_3$  binary library (reprinted from [42]).

films by Okazaki *et al* [42]. This system is believed to have potential applications in electro-optical devices. The results from the SEMM characterization are shown in figure 21. They identified the optimal composition to be  $x = 0.2\text{--}0.5$  and the best growth temperature to be  $650\text{--}700\text{ }^\circ\text{C}$ .

In order to search for high- $k$  gate dielectric materials for metal oxide semiconductor (MOS) devices, Okazaki *et al* [43] studied the dielectric properties of the amorphous  $\text{HfO}_2\text{--Y}_2\text{O}_3\text{--Al}_2\text{O}_3$  system. They deposited a ternary phase diagram composition spread on a Si substrate using the layer by layer combinatorial PLD technique. From the characterization using a SEMM, they found that the ternary

alloy  $\text{HfO}_2\text{:Y}_2\text{O}_3\text{:Al}_2\text{O}_3 = 6\text{:}1\text{:}3$  was the most promising gate oxide with the dielectric constant higher than those of single and binary oxides in this system. This alloy can also withstand post annealing at  $700\text{ }^\circ\text{C}$  for 30 min, which is crucial for real applications since the manufacturing of MOS devices involves high temperature processing.

Most recently, Takeuchi and co-workers applied the concept of multilayer composition spread to the combinatorial search for magnetoelectric (ME) materials [40]. As BTO and  $\text{CoFe}_2\text{O}_4$  (CFO) do not form a solid solution, they deposited the wedge layers in such a way that the thickness at the thick end of the wedges is an integral multiple ( $1\times$ ,  $3\times$ ,  $10\times$  and  $15\times$ ) of the unit cell of CFO. Although BTO and CFO have different structure types (pseudocubic with  $a = 0.403\text{ nm}$  for BTO and spinel cubic with  $a = 0.839\text{ nm}$  for CFO), the double unit cell of BTO matches the lattice constant of CFO, and their heteroepitaxial films were successfully grown on (100) MgO substrates. In this spread, the average composition changes continuously from pure BTO at one end to pure CFO at the other end.

A scanning x-ray diffractogram (figure 22) indicates that the (200) peak of BTO and the (400) peak of CFO evolve towards the middle of the spread continuously. The broadening of the peaks at the middle is also a clear evidence of intermixing and inter-diffusion at the interfaces and the distortion of the lattices.

Scanning SQUID microscopy and SEMM were used to characterize the magnetic and dielectric properties of the materials on the spread, as shown in figure 23. The dielectric constant decreases from 450 at the BTO end to 45 at the CFO end. The authors are currently using SEMM to perform characterization of the coupling between magnetism and ferroelectricity.

SEMM has also been used to study the effects of charge doping level, ionic radii and internal stress on a highly correlated-electronic/magnetic system by Yoo and his colleagues [20]. Using the same precursor PLD technique as Xiang [16], 108 different perovskite manganite  $\text{RE}_{1-x}\text{A}_x\text{MnO}_3$  (where RE is rare earth element Eu, Gd, Tb, Er, Tm

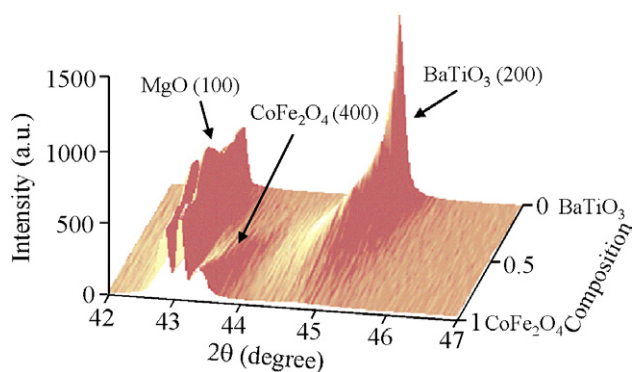


**Figure 22.** X-ray diffraction of a multilayer BTO–CFO composition spread on MgO.

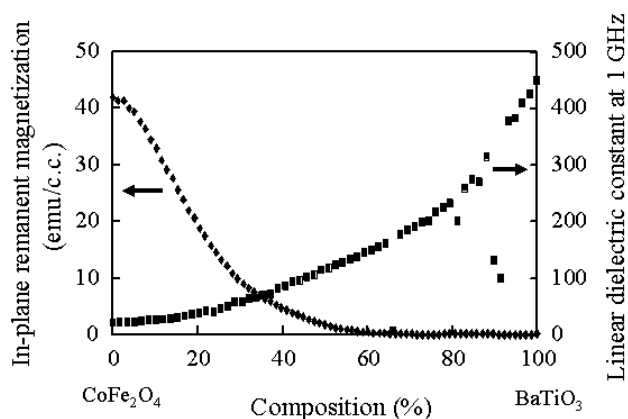


**Figure 23.** Relative dielectric constant and in-plane remanent magnetization of a CFO–BTO composition spread measured by SEMM and SQUID, respectively.

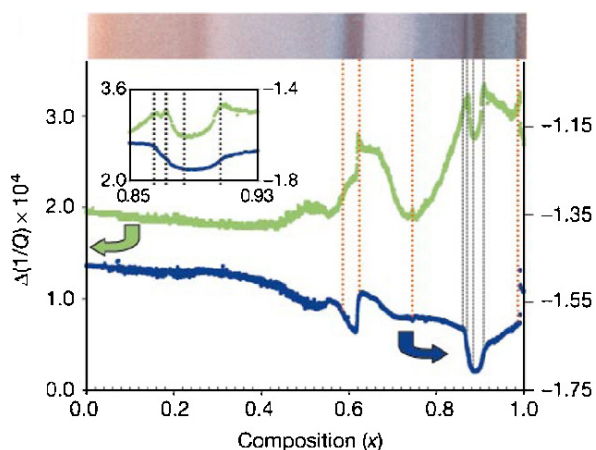


**Figure 24.** Electrical impedance of  $\text{Er}_{1-x}\text{Ca}_x\text{MnO}_3/\text{NdGaO}_3$  characterized using SEMM.

or Yb; A refers to Ca, Sr or Ba;  $x$  varies continuously from 0 to 1) binary continuous phase diagrams (CPD) were deposited on (100)  $\text{LaAlO}_3$ , (110)  $\text{NdGaO}_3$ , and (100)  $\text{SrTiO}_3$  substrates. Epitaxial films were obtained from precursors by appropriate *ex situ* post annealing processes, so that they can study the effect of different amounts of stress on the films induced by different substrates. Through characterization using SEMM and visible light reflection, they identified several extremely narrow phases (referred to as the singular phases)

with unusual electronic properties at room temperature. The peculiar properties were further found not to originate from atomic structural difference using x-ray diffraction, suggesting instead the occurrence of complicated electronic orderings as a function of  $x$ . Shown in figure 24 are typical data from SEMM and the reflection of  $\text{Er}_{1-x}\text{Ca}_x\text{MnO}_3/\text{NdGaO}_3$ . A detailed study was also performed on  $\text{La}_{1-x}\text{Ca}_x\text{MnO}_3/\text{LaAlO}_3$  [52]. Interested readers are directed to [54] for a detailed analysis of the electronic phase evolution studies in this experiment.

## 5. Summary

SEMM has been successfully implemented in high-throughput characterization of dielectric/ferroelectric materials libraries. The breakthrough in quantitative microscopy theory has played an important role in this progress. With further advances in theory and experimental techniques, we believe that SEMM will have even wider applications in high-throughput characterization of materials libraries for searching novel dielectric/ferroelectric materials, superconductors, semiconductors, magnetoelectric materials and opto-electrical materials.

## Acknowledgments

This work was supported by NSFC, CAS, MOE, NSRL and NSF DMR 0231291 and 094265.

## References

- [1] Xiang X D, Sun X D, Briceno G, Lou Y L, Wang K A, Chang H, Wallace-Freedman W G, Chen S W and Schultz P G 1995 A combinatorial approach to materials discovery *Science* **268** 1738–40
- [2] Kennedy K, Stefansky T, Davy G, Zackay V F and Parker E R 1965 Rapid method for determining ternary-alloy phase diagrams *J. Appl. Phys.* **36** 3808–10
- [3] Hanak J J 1970 The ‘multi-sample concept’ in materials research: synthesis, compositional analysis and testing of entire multicomponent systems *J. Mater. Sci.* **5** 964–71
- [4] Briceno G, Chang H, Sun X D, Schultz P G and Xiang X D 1995 A class of cobalt oxide magnetoresistance materials discovered with combinatorial synthesis *Science* **270** 273–5
- [5] Sun X D, Gao C, Wang J and Xiang X D 1997 Identification and optimization of advanced phosphors using combinatorial libraries *Appl. Phys. Lett.* **70** 3353–5
- [6] Danielson E, Golden J H, McFarland E W, Reaves C M, Weinberg W H and Wu X D 1997 A combinatorial approach to the discovery and optimization of luminescent materials *Nature* **389** 944–8
- [7] Danielson E, Devenney M, Giaquinta D M, Golden J H, Haushalter R C, McFarland E W, Poojary D M, Reaves C M, Weinberg W H and Wu X D 1998 A rare-earth phosphor containing one-dimensional chains identified through combinatorial methods *Science* **279** 837–9
- [8] Wang J, Yoo Y, Gao C, Takeuchi I, Sun X D, Chang H, Xiang X D and Schultz P G 1998 Identification of a blue photoluminescent composite material from a combinatorial library *Science* **279** 1712–4
- [9] Senkan S M 1998 High-throughput screening of solid-state catalyst libraries *Nature* **394** 350–3
- [10] Taylor S J and Morken J P 1998 Thermographic selection of effective catalysts from an encoded polymer-bound library *Science* **280** 267–70
- [11] Reddington E, Sapienza A, Gurau B, Viswanathan R, Sarangapani S, Smotkin E S and Mallouk T E 1998 Combinatorial electrochemistry: a highly parallel optical

- screening method for discovery of better electrocatalysts *Science* **280** 1735–7
- [12] Holzwarth A, Schmidt H W and Maier W F 1998 Detection of catalytic activity in combinatorial libraries of heterogeneous catalysts by ir thermography *Angew. Chem., Int. Ed. Engl.* **37** 2644–7
- [13] Cong P J, Doolen R D, Fan Q, Giaquinta D M, Guan S H, McFarland E W, Poojary D M, Self K, Turner H W and Weinberg W H 1999 High-throughput synthesis and screening of combinatorial heterogeneous catalyst libraries *Angew. Chem., Int. Ed. Engl.* **38** 484–8
- [14] Chang H, Gao C, Takeuchi I, Yoo Y, Wang J, Schultz P G, Xiang X D, Sharma R P, Downes M and Venkatesan T 1998 Combinatorial synthesis and high throughput evaluation of ferroelectric/dielectric thin-film libraries for microwave applications *Appl. Phys. Lett.* **72** 2185–7
- [15] Takeuchi I, Chang H, Gao C, Schultz P G, Xiang X D, Sharma R P, Downes M J and Venkatesan T 1998 Combinatorial synthesis and evaluation of epitaxial ferroelectric device libraries *Appl. Phys. Lett.* **73** 894–6
- [16] Chang H, Takeuchi I and Xiang X D 1999 A low-loss composition region identified from a thin-film composition spread of  $(\text{Ba}_{1-x}\text{Sr}_x\text{Ca}_y)\text{TiO}_3$  *Appl. Phys. Lett.* **74** 1165–7
- [17] van Dover R B, Schneemeyer L F and Fleming R M 1998 Discovery of a useful thin-film dielectric using a composition-spread approach *Nature* **392** 162–4
- [18] Akporiaye D E, Dahl I M, Karlsson A and Wendelbo R 1998 Combinatorial approach to the hydrothermal synthesis of zeolites *Angew. Chem., Int. Ed. Engl.* **37** 609–11
- [19] Klein J, Lehmann C W, Schmidt H W and Maier W F 1998 Combinatorial material libraries on the microgram scale with an example of hydrothermal synthesis *Angew. Chem., Int. Ed. Engl.* **37** 3369–72
- [20] Yoo Y K, Duewer F, Yang H, Yi D, Li J W and Xiang X D 2000 Room-temperature electronic phase transitions in the continuous phase diagrams of perovskite manganites *Nature* **406** 704–8
- [21] Syngé E H 1928 A suggested method for extending microscopic resolution into the ultra-microscopic region *Phil. Mag.* **6** 356–62
- [22] Frait Z 1959 The use of high-frequency modulation in studying ferromagnetic resonance *Czech. J. Phys.* **9** 403–4
- [23] Soohoo R F 1962 A microwave magnetic microscope *J. Appl. Phys.* **33** 1276–7
- [24] Ash E A and Nicholls G 1972 *Nature* **237** 510
- [25] Bryant C A and Gunn J B 1965 Noncontact technique for local measurement of semiconductor resistivity *Rev. Sci. Instrum.* **36** 1614–7
- [26] Fee M, Chu S and Hansch T W 1989 Scanning electromagnetic transmission line microscope with sub-wavelength resolution *Opt. Commun.* **69** 219–24
- [27] Gutmann R J, Borrego J M, Chakrabarti P and Wang M-S 1987 *IEEE MTT-S Digest* p 281
- Wang M S and Borrego J M 1990 *Mater. Eval.* **48** 1106
- [28] Tabib-Azar M, Su D P, Pohar A, LeClair S R and Ponchak G 1999 0.4  $\mu\text{m}$  spatial resolution with 1 GHz ( $\lambda = 30$  cm) evanescent microwave probe *Rev. Sci. Instrum.* **70** 1725–9
- [29] Wei T, Xiang X D, Wallace-Freedman W G and Schultz P G 1996 Scanning tip microwave near-field microscope *Appl. Phys. Lett.* **68** 3506–8
- [30] Aga R S, Brookman J, Dizon J and Wu J Z 2004 Development of a dual-channel scanning microwave optical microprobe *Appl. Phys. Lett.* **84** 1979–81
- [31] Novotny L, Pohl D W and Hecht B 1995 Scanning near-field optical probe with ultra small spot size *Opt. Lett.* **20** 970–2
- [32] Gao C, Hu B, Zhang P, Huang M M and Liu W H 2004 Quantitative microwave evanescent microscopy of dielectric thin films using a recursive image charge approach *Appl. Phys. Lett.* **84** 4647–9
- [33] Gao C, Wei T, Duewer F, Lu Y L and Xiang X D 1997 High spatial resolution quantitative microwave impedance microscopy by a scanning tip microwave near-field microscope *Appl. Phys. Lett.* **71** 1872–4
- [34] Gao C and Xiang X D 1998 Quantitative microwave near-field microscopy of dielectric properties *Rev. Sci. Instrum.* **69** 3846–51
- [35] Gao C, Duewer F and Xiang X D 1999 Quantitative microwave evanescent microscopy *Appl. Phys. Lett.* **75** 3005–7
- [36] Steinhauer D E, Vlahacos C P, Wellstood F C, Anlage S M, Canedy C, Ramesh R, Stanishevsky A and Melngailis J 2000 Quantitative imaging of dielectric permittivity and tunability with a near-field scanning microwave microscope *Rev. Sci. Instrum.* **71** 2751–8
- [37] Lee J H, Hyun S and Char K 2001 Quantitative analysis of scanning microwave microscopy on dielectric thin film by finite element calculation *Rev. Sci. Instrum.* **72** 1425–34
- [38] Wang Z, Kelly M A, Shen Z X, Wang G, Xiang X D and Wetzel J T 2002 Evanescent microwave probe measurement of low- $k$  dielectric films *J. Appl. Phys.* **92** 808–11
- [39] Chang K S, Aronova M, Famodu O, Takeuchi I, Lofland S E, Hattrick-Simpers J and Chang H 2001 Multimode quantitative scanning microwave microscopy of *in situ* grown epitaxial  $\text{Ba}_{1-x}\text{Sr}_x\text{TiO}_3$  composition spreads *Appl. Phys. Lett.* **79** 4411–3
- [40] Chang K S et al 2004 Exploration of artificial multiferroic thin-film heterostructures using composition spreads *Appl. Phys. Lett.* **84** 3091–3
- [41] Minami H, Itaka K, Ahmet P, Komiyama D, Chikyow T, Lippmaa M and Koinuma H 2002 Rapid synthesis and scanning probe analysis of  $\text{Ba}_x\text{Sr}_{1-x}\text{TiO}_3$  composition spread films on a temperature gradient Si(100) substrate *Japan. J. Appl. Phys.* **2** 42 L149–51
- [42] Okazaki N et al 2002 Development of scanning microwave microscope with a lumped-constant resonator probe for high-throughput characterization of combinatorial dielectric materials *Appl. Surf. Sci.* **189** 222–6
- [43] Okazaki N et al 2004 Characterization of  $\text{LiNb}_{1-x}\text{Ta}_x\text{O}_3$  composition-spread thin film by the scanning microwave microscope *Appl. Surf. Sci.* **223** 196–9
- [44] Hasegawa K, Ahmet P, Okazaki N, Hasegawa T, Fujimoto K, Watanabe M, Chikyow T and Koinuma H 2004 Amorphous stability of  $\text{HfO}_2$  based ternary and binary composition spread oxide films as alternative gate dielectrics *Appl. Surf. Sci.* **223** 229–32
- [45] Pozar D M 1990 *Microwave Engineering* (New York: Addison-Wesley)
- [46] Kajfez D and Guillon P 1998 *Dielectric Resonators* 2nd edn (Atlanta, GA: Noble)
- [47] Gao C, Duewer F, Lu Y-L and Xiang X-D 1998 Quantitative nonlinear dielectric microscopy of periodically polarized ferroelectric domains *Appl. Phys. Lett.* **73** 1146–8
- [48] Knauss L A, Pond J M, Horwitz J S, Chrisey D B, Mueller C H and Treece R 1996 The effect of annealing on the structure and dielectric properties of  $\text{Ba}_x\text{Sr}_{1-x}\text{TiO}_3$  ferroelectric thin films *Appl. Phys. Lett.* **69** 25–7
- [49] Varadan V K, Gohdgaonkar D K, Varadan V V, Kelly J F and Glikerdas P 1992 Ceramic phase shifters for electronically steerable antenna systems *Microw. J.* **35** 116
- [50] Horikawa T, Mikami N, Makita T, Tanimura J, Kataoka M, Sato K and Nunoshita M 1993 Dielectric-properties of  $(\text{Ba}, \text{Sr})\text{TiO}_3$  thin-films deposited by rf-sputtering *Japan. J. Appl. Phys.* **1** 32 4126–30
- [51] Scott J F 1995 Dielectric-breakdown in high-epsilon films for ULSI DRAMs: 3. Leakage current precursors and electrodes *Integr. Ferroelectr.* **9** 1–12
- [52] Yoo Y K et al 2001 Strong correlation between high-temperature electronic and low-temperature magnetic ordering in  $\text{La}_{1-x}\text{Ca}_x\text{MnO}_3$  continuous phase diagram *Phys. Rev. B* **63** 224421